Mayser, J. P., Flecker, R., Marzocchi, A., Kouwenhoven, T., Lunt, D., & Pancost, R. (2017). Precession driven changes in terrestrial organic matter input to the Eastern Mediterranean leading up to the Messinian Salinity Crisis. *Earth and Planetary Science Letters*, *462*, 199-211. https://doi.org/10.1016/j.epsl.2017.01.029

Precession driven changes in terrestrial organic matter input to the Eastern Mediterranean leading up to the Messinian Salinity Crisis

Jan Peter Mayser [a,b,*], Rachel Flecker [b,c], Alice Marzocchi [b,c,1] , Tanja J. Kouwenhoven [d], Dan J. Lunt [b,c], Rich D. Pancost [a,b]

[a] Organic Geochemistry Unit, School of Chemistry, University of Bristol, Cantock's Close, Bristol BS8 1TS, UK

[b] BRIDGE, School of Geographical Sciences, University of Bristol, University Road, Bristol BS8 1SS, UK

[c] Cabot Institute, University of Bristol, Bristol BS8 1UJ, UK

[d] Department of Geosciences, Utrecht University, Heidelberglaan 2, 3584 CS Utrecht, The Netherlands

Abstract

Eastern Mediterranean sediments over the past 12 Myr commonly show strongly developed precessional cyclicity, thought to be a biogeochemical response to insolation-driven freshwater input from run-off. The Mediterranean's dominant freshwater source today and in the past, is the Nile, which is fed by North African monsoon rain; other, smaller, circum-Mediterranean rivers also contribute to Mediterranean hydrology. Crucially, run-off through all of these systems appears to vary with precession, but there is no direct evidence linking

[1] current address: Department of the Geophysical Sciences, The University of Chicago, USA

21 individual water sources to the biogeochemical response recorded in Mediterranean
22 sediments. Consequently, it is not clear whether the North African monsoon is entirely
23 responsible for the Mediterranean's sedimentary cyclicity, or whether other, precessional
24 signals, such as Atlantic storm precipitation, drive it.

25 Organic matter in sediments derives from both marine and terrestrial sources and
26 biomarker analysis can be used to discriminate between the two, thereby providing insight
27 into sedimentary and ecological processes. We analysed a wide range of lipids from the Late
28 Miocene (6.6-5.9 Ma) Pissouri section, southern Cyprus, and reconstructed the vegetation
29 supplied to this region by measuring the carbon isotopes of the terrestrial component to
30 identify its geographic source. BIT (Branched-Isoprenoidal-Tetraether) indices reflect changes
31 in the relative abundance of marine vs terrestrial (soil) organic matter inputs, and with the
32 exception of records from the last deglaciation, this work is the first application of the BIT
33 approach to the reconstruction of orbital impacts on sedimentological processes. BIT indices
34 show that the organic matter supplied to Cyprus changed over the course of each precession
35 cycle and was dominantly terrestrial during insolation maxima when North African run-off was
36 enhanced. The $\delta^{13}C$ values from these intervals are compatible with tropical North African
37 vegetation. However, the $\delta^{13}C$ record indicates that during insolation minima, organic material
38 supplied to southern Cyprus derives from a more arid source region. This is likely to have been
39 aeolian-transported organic matter from the Anatolian Plateau demonstrating that even in
40 Mediterranean sedimentary systems influenced by Nile run-off, there is more than one
41 independent precessional organic matter contribution to the sedimentary cyclicity. Pissouri's
42 organic geochemistry also illustrates a long-term trend towards more saline Mediterranean
43 conditions during the 600 kyr leading up to the Messinian Salinity Crisis.

Highlights

- BIT index shows major precessional changes in run-off to the Mediterranean.
- $\delta^{13}C$ record of higher plant waxes also varies with precession
- Cyprus receives organic matter input from both North Africa and Turkey
- New SST record leading up to the Messinian Salinity Crisis
- Long-term biomarker trends indicate the looming Messinian Salinity Crisis

Keywords:

Mediterranean; BIT index; carbon isotopes; Messinian Salinity Crisis; terrestrial higher plant waxes; TEX_{86}

1 Introduction

Mediterranean sedimentary successions over the last 12 million years (Ma) are commonly dominated by strong cyclicity (Kidd et al., 1978; Rohling et al., 2015). These regular lithological alternations, comprising some combination of marls, limestones, diatomites and organic-rich sapropelic layers, are demonstrably precessional (Hilgen et al., 1997; Sierro et al., 2001) and are thought to be the Mediterranean's biogeochemical response to orbitally-driven variations in freshwater input (Rossignol-Strick, 1985). The largest source of this freshwater variation is derived from the North African monsoon (Rohling et al., 2015 and references therein). Precessional changes shift the position of the Intertropical Convergence Zone (ITCZ) northward during times of insolation maxima (July 65N; Laskar et al., 2004) and increase the intensity of the monsoon in the catchment of northward draining rivers that flow into the Mediterranean (Marzocchi et al., 2015). These insolation-driven changes also affect the vegetation across North Africa (Larrasoaña et al., 2013), although model simulations fail to

66 capture the full greening of the Sahara indicated by terrestrial data (Larrasoaña et al., 2013
67 and references therein). Precessional changes in the location and intensity of North Atlantic
68 storm tracks also impact Mediterranean precipitation patterns, principally in the west and
69 along the north Mediterranean margin (Kutzbach et al., 2014; Toucanne et al., 2015).

70 In the Late Miocene Mediterranean salinity rose significantly and thick, basin-wide
71 evaporites were deposited during the Messinian Salinity Crisis (MSC, 5.971-5.33 Ma; Manzi et
72 al., 2013 and references therein). While deep basinal evaporites have yet to be recovered,
73 those preserved on the Mediterranean margins also show strong cyclicity which is thought to
74 reflect an on-going precessional signal (Flecker et al., 2015), despite extreme environmental
75 conditions. Although the transition to evaporite precipitation in the Mediterranean is
76 synchronous and abrupt at 5.97 Ma (Manzi et al., 2013), geochemical evidence (Flecker et al.,
77 2015 and references therein) as well as water column oxygenation and faunal data
78 (Kouwenhoven et al., 2003; Sierro et al., 2001) indicate that the first environmental precursors
79 of the MSC occurred several million years earlier.

80 The evidence of precessional-pacing of Mediterranean sedimentation is clear. However,
81 the specific processes that generated the recorded biogeochemical response remain
82 controversial. Debates over the role of freshwater driven productivity versus water column
83 stratification in the generation of organic-rich sapropelic layers (Kidd et al., 1978) endure,
84 while the question of whether deep-sea anoxia, promoted by enhanced export productivity,
85 a freshwater cap, or a combination of both, can transfer the precessional run-off signal from
86 the Eastern to Western Basins as advocated by Rohling et al. (2015), remains untested. One
87 alternative possibility is that the North Atlantic storm-track generates the precessional
88 biogeochemical response in the Western Mediterranean independent of, but in phase with
89 precessional run-off to the Eastern Mediterranean (Toucanne at al. 2015). However, it is not

clear whether the storm track precipitation is volumetrically sufficient to generate the biogeochemical response observed.

All of these controversies relate, in part, to the difficulty in identifying the fresh water sources responsible for driving the biogeochemical sedimentary product observed in the Mediterranean Basin. This study uses biomarkers preserved within the sedimentary record as tracers of the freshwater from which they were derived in order to explore and provide new insight into the underlying dynamics of the Mediterranean's sedimentary cyclicity.

Lipid biomarkers have been used to explore changes in the hydrological cycle in a variety of ways. Leaf wax $\delta^{13}C$ values differ between C_3-and C_4-plants where C_3-plants have lower $\delta^{13}C$ values than C_4-plants (O'Leary, 1981) as a result of their different morphology and carbon assimilation biochemistry (Edwards et al., 2010 and references therein). Because the distribution of C_3- and C_4-plants is governed by a combination of environmental factors, including temperature and aridity (Yang et al., 2014), leaf wax $\delta^{13}C$ values provide insight into both past vegetation and climatic conditions. Biomarkers can also provide insight into changes in marine versus terrestrial organic matter (OM) fluxes (Hopmans et al., 2004), from which changes in the OM source can be inferred. Other lipid biomarkers, including isoprenoidal and branched glycerol dialkyl glycerol tetraether (GDGT) lipids can be used to determine sea-surface temperatures ($TEX_{86,}$ [TetraEther indeX]; Schouten et al., 2013 and references therein) and land surface temperatures (MBT' [Methylation of Branched Tetraether]/CBT [Cyclisation of Branched Tetraethers]; Weijers et al., 2007; Peterse et al., 2012), providing additional insights into environmental changes. This approach constrains the relative control of temperature versus aridity on C_3/C_4 plant abundances.

We have applied these approaches to the Late Miocene Pissouri section on Cyprus (5.98-6.51 Ma), which lies to the north of the Nile delta (Fig. 1). Today, the majority of the

114 monsoon-derived North African run-off reaches the Mediterranean via the Nile which is its
115 largest fluvial system. We extracted and characterised biomarkers from the strongly cyclic
116 Pissouri succession and have used them to reconstruct the influence of Nile water and the
117 precipitation in its catchment. In particular, we use the proportions branched-GDGTs
118 (brGDGTs) to crenarchaeol (BIT index), distributions of *n*-alkyl lipids, and the $\delta^{13}C$ values of
119 high molecular weight *n*-alkanes of terrestrial plant origin, to establish the nature of organic
120 matter supplied to this central eastern Mediterranean region. The ~600 kyr interval preceding
121 the MSC was targeted in order to evaluate the climatic changes that occur during the leading
122 up to the MSC.

123 **2 Methods**

124 ***2.1 Site description and sampling strategy***

125 The Pissouri basin on southern Cyprus (Fig. 1) is filled with Neogene sediments
126 extending back to the Middle Miocene (Krijgsman et al., 2002). The Messinian succession of
127 the basin comprises regular alternations of limestones and marls (Fig. 2; Krijgsman et al.,
128 2002) where carbonate content (Krijgsman et al., 2002) has been used to distinguish them
129 (e.g. limestone >75%; marl <75%; Sugden and McKerrow, 1962). The cyclicity of the succession
130 has been used to astronomically tune the Pissouri section to orbital solutions (Laskar et al.,
131 2004) using both bio- and magnetostratigraphic tie-points (Fig. 2; Krijgsman et al., 2002). At
132 Pissouri, three biostratigraphic events occur in the 30 m of limestone-marl alternations that
133 directly underlie the gypsum and are studied here (Fig. 2). These biostratigraphic tie points
134 consistently link marl deposition to the area of the orbital curve that includes the insolation
135 maxima (Fig. 2). In addition, three magnetostratigraphic boundaries also occur in this part of
136 the section (Fig. 2) and these are consistent with the tuning based on biostratigraphic tie-

points and confirm the lithological phase relationship with the orbital curve (Krijgsman et al., 2002). The marls have been correlated with sapropelic horizons (Krijgsman et al., 2002) that are observed in other Mediterranean successions (e.g. Sorbas; Sierro et al., 2001). In line with standard practice for astronomically tuned Mediterranean successions and consistent with the biostratigraphic and magnetostratigraphic tie points, the middle of each marl (or sapropel) layer is linked to the extremes of the 65N summer insolation curve (Sierro et al., 2001; Fig 2.).

Forty-eight samples were collected in 1998 from the Pissouri section road cut (Kouwenhoven et al., 2006; Krijgsman et al., 2002) before it was sprayed with concrete. Where possible, one sample for every limestone and one for every marl was analysed throughout the section, starting at ~32 m below the gypsum and representing the 600 kyr preceding the MSC (6.519- 5.983; Ma Krijgsman et al., 2002). While this approach does not necessarily show the full range of values in relation to precession, it does allow us to compare data generated during two distinct phases of multiple orbital cycles. The slump layer (7-10 m Fig. 2) towards the top of the section was not sampled because its age and orbital phasing is uncertain.

2.2 Extraction and Separation

The sediments (~40g) were homogenised and extracted via Soxhlet apparatus for 24 hours using dichloromethane (DCM): methanol (MeOH) (2:1 vol/vol). An aliquot of the total lipid extract (TLE) was separated into two fractions using alumina flash column chromatography: an apolar fraction eluted with 4 ml hexane (Hex)/DCM (9:1 v/v) and a polar fraction eluted with 3 ml DCM:MeOH (1:2 vol/vol). An internal standard (IS) was added to the apolar (androstane 5µl of 200 ng/µl) and polar (hexadecan-2-ol, 5 µl, 207.5 mg/µl solution) fractions. The polar fraction was derivatised for 1 hour at 70°C using 50µl of BSTFA+TMCS 99:1 (N,O-bis(trimethylsilyl) trifluoroacetamide and trimethylchlorosilane).

2.3 GC-MS

Both fractions were analysed using a Thermo Scientific ISQ Single Quadrupole gas chromatography-mass spectrometer (GC-MS). The GC was equipped with a 50 m x 0.32 mm i.d. fused silica capillary column with an Rtx-1 stationary phase (100% dimethylpolysiloxane, 0.17 µm film thickness; Restek) and programmed from 70 °C (held for 1 minute) to 130 °C at 20 °C/minute, then to 300 °C (held for 24 minutes) at 4 °C/minute. The MS continuously scanned between mass to charge ratios *m/z* 50 and 650 Daltons. The *n*-alkanes, *n*-alkanols and *n*-alkanoic acids were identified by their spectra and quantified in the total ion current.

2.3.1 GC-C-IRMS

The *n*-alkane $\delta^{13}C$ values were determined using an Isoprime 100 GC-combustion-isotope ratio MS (GC-C-IRMS). Apolar fractions were analysed in duplicate, injected via a splitless injector onto a 50 m x 0.32 i.d. fused silica capillary column with an HP 1 stationary phase (100% dimethylpolysiloxane, 0.17 film thickness, Agilent). The temperature programme was the same as for GC-MS analysis. The combustion reactor was maintained at a temperature of 850 °C. Standard notation relative to the Vienna Pee Dee Belemnite (VPDB) was achieved by comparison against a calibrated reference CO_2 gas. Two thirds of samples had sufficient *n*-alkane abundances for $\delta^{13}C$ determination.

2.3.2 HPLC-APCI-MS

The second aliquot of the TLE was dissolved in A (A=hexane:iso-propanol (IPA) (99:1 v/v)) and passed through a 0.45 µm PTFE filter. High performance liquid chromatography-atmospheric pressure chemical ionisation-MS (HPLC-APCI-MS) was performed using a ThermoFisher Scientific Accela Quantum Access triple quadrupole MS to analyse the iGDGTs and brGDGTs. Separation was achieved with an Alltech Prevail Cyao column (150 mm; 2.1 mm;

3µm i.d.) with a flow rate of 0.2 ml/minute. The initial solvent mix A was eluted isocratically for 5 minute, followed by a change in solvent polarity via a gradient to 1.8% IPA over 45 minutes (Hopmans et al., 2000). After separation, ionisation was performed at atmospheric pressure, and select *m/z*: 1302, 1300, 1298, 1296, 1294, 1292, 1050, 1048, 1046, 1036, 1034, 1032, 1022, 1020, 1018, 744, 659 (Fig.3; Schouten et al., 2013) were scanned to increase sensitivity and reproducibility. GDGT ratios were calculated from the respective M^+-ions chromatograms, and abundances were determined by comparing with a known C_{46}-GDGT standard (Huguet et al., 2006). The relative response of the standard and the GDGTs was not determined, such that reported concentrations are strictly semi-quantitative.

2.3.3 Proxies

Long-chain *n*-alkanes are synthesised by terrestrial vascular plants (Eglinton and Hamilton, 1967). The carbon preference index (CPI) is the ratio of odd-to-even chain lengths of the *n*-alkanes and is calculated as follows:

$$\mathrm{CPI} = 0.5 * \left(\frac{\mathrm{C_{23}} + \mathrm{C_{25}} + \mathrm{C_{27}} + \mathrm{C_{29}} + \mathrm{C_{31}} + \mathrm{C_{33}}}{\mathrm{C_{24}} + \mathrm{C_{26}} + \mathrm{C_{28}} + \mathrm{C_{30}} + \mathrm{C_{32}} + \mathrm{C_{34}}} + \frac{\mathrm{C_{23}} + \mathrm{C_{25}} + \mathrm{C_{27}} + \mathrm{C_{29}} + \mathrm{C_{31}} + \mathrm{C_{33}}}{\mathrm{C_{22}} + \mathrm{C_{24}} + \mathrm{C_{26}} + \mathrm{C_{28}} + \mathrm{C_{30}} + \mathrm{C_{32}}}\right)$$

Equation 1: CPI (Bray and Evans, 1961)

The components of Equation 1 refer to the relative concentrations of C_{22} to C_{32} *n*-alkanes. During biosynthesis, higher plants produce high-molecular-weight (HMW) odd-numbered *n*-alkanes (Eglinton and Hamilton, 1967), but subsequent diagenesis (and catagenesis) causes homogenisation of the distribution (Bray and Evans, 1961). Consequently, lower CPI values can indicate increased degradation of these terrestrial inputs or a change in their source, whereas values >2 indicate good preservation.

The terrestrial aquatic ratio ($TAR_{n\text{-alkanes}}$) for the *n*-alkanes is calculated as:

$$\mathrm{TAR}_{n-\mathrm{alkanes}} = \frac{\mathrm{C_{27}} + \mathrm{C_{29}} + \mathrm{C_{31}}}{\mathrm{C_{15}} + \mathrm{C_{17}} + \mathrm{C_{19}}}$$

Equation 2: TAR (Bourbonniere and Meyers, 1996)

205 This can be used to evaluate sources of OM, because HMW *n*-alkanes are generally
206 produced by terrestrial vascular plants (Eglinton and Hamilton, 1967), and low-molecular-
207 weight (LMW) *n*-alkanes generally derive from aquatic organisms (Meyers and Arnaboldi,
208 2008 and references therein). Similar ratios can be calculated using *n*-alkanoic acids
209 (Bourbonniere and Meyers, 1996):

210 $$\mathrm{TAR}_{n-\mathrm{alkanoic\ acids}} = \frac{\mathrm{C}_{26} + \mathrm{C}_{28}}{\mathrm{C}_{14} + \mathrm{C}_{16} + \mathrm{C}_{18}}$$

Equation 3: $TAR_{n\text{-alkanoic acids}}$ (Bourbonniere and Meyers, 1996)

211 The BIT index is a ratio of the three major brGDGTs to crenarchaeol:

212 $$\mathrm{BIT} = \frac{(\mathrm{GDGT-Ia}) + (\mathrm{GDGT-IIa}) + (\mathrm{GDGT-IIIa})}{(\mathrm{Crenarcheaol}) + (\mathrm{GDGT-Ia}) + (\mathrm{GDGT-IIa}) + (\mathrm{GDGT-IIIa})}$$

Equation 4: BIT Index (Hopmans et al., 2004)

213 Crenarchaeol is derived from Thaumarchaeota (Sinninghe Damsté et al., 2002), which
214 represents ~20% of the picoplankton in the ocean, although it also occurs in subordinate
215 abundances in soils (Weijers et al., 2007). BrGDGTs occur in high abundances in terrestrial
216 settings, including soils and peats (Hopmans et al., 2004; Peterse et al., 2012). Therefore, BIT
217 indices close to 1 represent OM originating from a predominantly terrigenous source, whereas
218 low indices represent a Thaumarchaeotal source of GDGTs and by extension a strong aquatic
219 source of OM (Schouten et al., 2013).

220 For the sea-surface temperature reconstructions, the TEX_{86} proxy is defined as:

221 $$\mathrm{TEX}_{86} = \frac{\mathrm{GDGT-2} + \mathrm{GDGT-3} + \mathrm{Crenarcheaol'}}{\mathrm{GDGT-1} + \mathrm{GDGT-2} + \mathrm{GDGT-3} + \mathrm{Crenarcheaol'}}$$

Equation 5: TEX_{86}-proxy (Schouten et al., 2013)

222 Various calibrations have been proposed to transform TEX_{86} values to sea-surface

temperature (SST), including both the original linear (Schouten et al., 2013) and subsequent logarithmic (Kim et al., 2010) relationships. Here, we use the BAYSPAR-calibration, which enables an increased accuracy and precision of reconstructions, due to the inclusion of a spatial element in the calibration (Tierney and Tingley, 2015), as well as more robust Bayesian-derived error estimates. It applies the modern core-top data and searches for modern analogue locations based on the TEX_{86} index (Tierney and Tingley, 2015). Biomarker data (i.e. hopane distributions) indicate that Pissouri OM is thermally immature, justifying the application of this core-top approach to these uplifted marine sediments.

For the land-based temperature reconstructions the MBT'/CBT index is used:

$$\mathrm{CBT} = \log \frac{\mathrm{GDGTIb} + \mathrm{GDGTIIb}}{\mathrm{GDGTIa} + \mathrm{GDGTIIa}}$$

$$\mathrm{MBT'} = \frac{\mathrm{GDGTIa} + \mathrm{GDGTIb} + \mathrm{GDGTIc}}{\mathrm{GDGTIa} + \mathrm{GDGTIb} + \mathrm{GDGTIc} + \mathrm{GDGTIIa} + \mathrm{GDGTIIb} + \mathrm{GDGTIIc} + \mathrm{GDGTIIIa}}$$

Equation 6: MBT'/CBT proxy (Peterse et al., 2012)

In soils, the degree of cyclisation of branched GDGTs (reflected in the CBT index) is correlated with pH, whereas the degree of methylation (MBT') is correlated with both pH and Mean Annual Air Temperature (MAAT), resulting in the MBT(')/CBT soil temperature proxy (Weijers et al., 2007, Peterse et al., 2012). This proxy is commonly applied to marginal marine sediments to reconstruct the terrestrial climate of the catchment area (e.g. Peterse et al., 2012). Since these analysis were completed, a new methodology has been proposed by De Jonge et al. (2014) to include 6-methyl brGDGTs as well as the 5-methyl brGDGTs in the CBT and MBT' proxies. GDGT abundances are low in these Pissouri samples, so there was insufficient material to enable reanalysis and the application of this new method.

3 Results

All samples contained a variety of biomarkers, including both branched (brGDGT) and isoprenoidal (iGDGT) GDGTs (Fig. 3) and a homologous series of *n*-alkanes and *n*-alkanoic acids. Also present was an unusual nonacosan-10-ol which can be derived from conifers (Jetter and Riederer, 1995).

3.1 GDGTs

The Pissouri sediments contain a wide range of br- and iGDGTs (Fig. 3; data table; Schouten et al., 2013). BIT indices are highly variable in the Pissouri sediments (Fig. 4c), ranging from below 0.1 to 0.85, indicating more than one OM source. These variations are strongly related to lithology, where the marls have significantly higher (Student's paired t-test between BIT values of marls vs limestones $p<0.0001$) BIT indices (0.3 to 0.9) than the limestones (0.1 to 0.6; Fig. 4c). There is a general decline in the limestone BIT indices from 0.6 to 0.05, up section (Fig. 4c). BIT indices from the marls have a more complex pattern, with high BIT indices (0.67-0.90) in sediments older than 6.26 Ma and in those overlying the slump (0.67-0.88) and lower indices in the intervening interval (0.17-0.65). Consequently, the difference in marl-limestone BIT indices is most pronounced at the top and bottom of the section, with a smaller marl-limestone contrast in BIT indices between 6.3 Ma and the slump (Fig. 4c), mainly due to lower values in the marls.

The low BIT-contrast interval immediately below the slump is also characterised by variable i- and brGDGTs abundances (Fig. 4d), with some values approximately two orders of magnitude higher than in the rest of the section.

Br- and iGDGTs can also be used to determine terrestrial and sea-surface temperatures (see Section 2.3.3). However, TEX_{86} should not be applied to sediments with high BIT indices (>0.4; Schouten et al., 2013 and references therein), and terrestrial temperatures should be

267 treated with caution in samples with low (<0.3, Weijers et al., 2007) BIT indices. In the Pissouri
268 section, 24 samples had BIT indices lower than 0.4, indicating the dominance of marine GDGTs
269 (Hopmans et al., 2004); in these, the TEX_{86}-derived SSTs range from 22°-30°C (data table) using
270 the BAYSPAR calibration (Tierney and Tingley, 2015). The 32 samples with BIT indices > 0.3,
271 yield MBT'/CBT-derived MAAT for the adjacent land ranging from 15° to 28° C (data table)
272 based on the calibration of (Peterse et al., 2012).

273 ***3.2 N-alkyl biomarkers***

274 The overall distribution of the *n*-alkanoic acids in the Pissouri samples is bimodal, with
275 a peak at *n*-C_{16} and a second peak at *n*-C_{28}. In most cases the *n*-C_{28} *n*-alkanoic acid is most
276 abundant. The $TAR_{n\text{-alkanoic acid}}$ values vary from 0.7 to 2.2 (Fig. 5e). Commonly the limestones
277 have lower TARs than the marl layers (Fig. 5e), but this difference is less consistent than in the
278 BIT indices (Fig. 4c).

279 The *n*-alkane distribution is similar to the bimodal *n*-alkanoic acid distribution with one
280 short-chain peak (C_{19} although C_{15} and C_{17} homologues are also abundant) and another long-
281 chain maximum (C_{31}). The concentrations of the HMW *n*-alkanes range between 0.6 and 12
282 ng/g sediment (Fig. 5a), and is generally lower in the limestones. Between 6.35 and 6.15 Ma
283 the offset between the two lithologies is particularly clear, with higher *n*-alkane
284 concentrations occurring in the marls (Fig. 5a). The $TAR_{n\text{-alkanes}}$ ratio (data table) varies from
285 0.05 to 3.16 with an average of 0.36, but unlike the BIT indices, the $TAR_{n\text{-alkanes}}$ (Fig. 5b) show
286 no systematic relationship with lithology, potentially due to the complex range of biological
287 sources for the LMW components or a diverse range of higher plant inputs (i.e. aeolian vs
288 fluvial inputs) for the HMW components. At the top of the section, the $TAR_{n\text{-alkanes}}$ shift to
289 higher indices, i.e. higher concentrations of long chain *n*-alkanes indicating stronger terrestrial

290 inputs (Fig. 5b).

291 With one exception, all sediments have a CPI >1 (Fig. 5d; data table) with an average
292 value of 6 and a range from 2 to 8. This indicates a strong predominance of odd-over-even
293 HMW *n*-alkanes, compatible with a leaf wax source and good preservation (Bray and Evans,
294 1961). We have excluded the sample at 6.11 Ma (R.F.-7013f; data table) from further
295 discussion, because of its anomalously low CPI and position close to the slump interval.

296 Nonacosan-10-ol, which is derived from specific conifers (Jetter and Riederer, 1995), is
297 found throughout the section (Fig. 5c). Concentrations do not vary systematically with
298 lithology, but, with the exception of one highly concentrated sample at 6.2 Ma, the relatively
299 constant Nonacosan-10-ol concentration that characterises the lower part of the succession
300 up to 6.1 Ma is followed by a trend towards higher concentrations (6.08 - 5.98 Ma).

301 **3.3 Carbon isotopes of the long-chain *n*-alkanes**

302 In the Pissouri section, $\delta^{13}C$ values for the HMW C_{29}, C_{31} and C_{33} *n*-alkanes (Fig. 6) range
303 between -35‰ and -26‰. This range is more negative than the $\delta^{13}C$ values typically
304 associated with leaf waxes from C_4-plants (Kohn, 2016 and references therein), but is
305 consistent both with $\delta^{13}C$ values measured on C_3 plants or a mixture of C_4 and C_3 plants (Fig.
306 6). In the upper part of the section (younger than 6.22 Ma), $\delta^{13}C$ values for all three long-chain
307 *n*-alkanes are consistently lower by 2-3‰ in the limestones, than in the marls with which they
308 are interbedded (Fig. 6). In the lower part of the section low *n*-alkane abundances prevented
309 $\delta^{13}C$ analysis in 10 samples (~21% of dataset). However, where measured, *n*-alkanes in
310 limestones have lower $\delta^{13}C$ values than those in the adjacent marls.

4 Discussion

4.1 Temperature proxies

As discussed above, GDGTs are used to reconstruct both land and marine palaeo-temperatures. The high variability of marine versus terrestrial source inputs (Fig. 7a) at Pissouri allows both the marine and the terrestrial temperatures to be evaluated but only for specific horizons. Where BIT indices are <0.4 (Fig. 7b; Schouten et al., 2013 and references therein), TEX_{86}-derived SSTs are in good agreement with alkenone-derived SST records from Monte dei Corvi, Italy (Tzanova et al., 2015; Fig. 7a). The combined datasets indicate a cooling of the Eastern Mediterranean prior to the onset of the MSC (Fig. 7), consistent with a global Late Miocene cooling (Herbert et al, 2016). The average temperature of the Eastern Mediterranean today is 20-22°C, several degrees cooler than that indicated by the average SST for these Late Miocene samples (25.5°C; Fig. 7a) even when including the TEX_{86} uncertainty of 2-3° (Tierney and Tingley, 2015). The long-term temperature change is overprinted by shorter-term variability of 6°C (Fig. 7). The 12-13 kyr resolution of both our TEX_{86} and the alkenone (Tzanova et al., 2015) datasets means that we cannot be sure that this reflects the full range of precessional temperature variability.

The terrestrial MBT'/CBT-derived MAAT records appear to suggest an average temperature of 18°C with large temperature variations of up to 14°C (Fig. 7c); much larger than those seen in the SST reconstruction (Fig. 7a). However, the average is lower than that observed today (20°C) and the large variability is unexpected, even given the large standard error on MBT'/CBT-derived MAAT reconstructions of +/- 5°C (Peterse et al., 2012). There are several likely reasons for the pronounced variations.

1. New analytical methods have been developed (De Jonge et al., 2014), and these could affect both determination of MBT indices and the application of appropriate calibrations.

We consider this factor to be minor given that much previous work based on the original methods and calibrations still exhibited clear temporal trends.

2. The dataset includes samples with low BIT indices, which could be problematic (Weijers et al., 2007); however, removing those data with BIT below 0.3 yields an average MAAT of 18°C and a range of 15° to 28°C, still much larger than expected.
3. Recent work has repeatedly shown that MBT'/CBT indices yield relatively low MAATs in arid settings (Peterse et al., 2012; Yang et al., 2014). Using a recently developed aridity calibration, shifts the temperatures to higher values by ~ 2°C (Yang et al., 2014), and given the fact that aridity is likely to have varied in the source region, this could be another source of variability.

Overall, it appears that GDGT-based proxies confirm that the Eastern Mediterranean was warmer during the Lateiocene than it is today, consistent with globally higher temperatures (e.g. Tzanova et al., 2015) and model simulations using elevated pCO_2 (Marzocchi et al., 2015). Elevated MAATs are less clear, given the profound variability in brGDGT indices, but we attribute this to complex changes in sources of brGDGTs and the additional impact of highly variable hydrology (Yang et al., 2014).

4.2 Differences in limestone and marl OM inputs

There is a statistically significant difference between the BIT indices of the limestones and those of the marls (P>0.001; students t-test; Fig. 4c), probably as a result of varying OM sources and preservation controls. The BIT index can be affected by OM degradation, with preferential degradation of marine OM over terrestrial OM shifting BIT indices higher (Huguet et al, 2009). Indeed, enhanced preservation beneath the slump is suggested by the higher GDGT concentrations (Fig. 4d) and this may account for the abrupt shift to lower BIT indices

358 in the marls from this interval (Fig. 4c). In other intervals, however, the GDGT concentrations
359 exhibit much less variability and no systematic change with lithology suggesting that
360 differential OM degradation is not the primary driver of cyclic BIT variations. This is consistent
361 with previous work where Huguet et al. (2009) showed that extreme changes in redox
362 conditions, between oxic and anoxic sediments with the same OM input, can result in changes
363 in the BIT index preserved, but only by up to 0.4. The BIT variations we see here are >0.4 and
364 therefore cannot be entirely attributable to oxic degradation. In addition, the presence of
365 benthic foraminifera in both limestones and marls (Kouwenhoven et al., 2006) suggests that
366 oxygen fluctuations were never extreme enough to induce total anoxia. Elevated proportions
367 of the benthic foraminifera, *Bolivina spathulata* (70-90%), however, indicate that, as early as
368 7.167 Ma the sediments were also never fully oxic , and changes in redox conditions from less
369 to more severe dysoxia on a precessional time scale are apparent from repeated shifts in
370 benthic foraminifer assemblages after 6.4 Ma (Kouwenhoven et al., 2006 and references
371 therein). Consequently, the redox-driven preservational impact on BIT indices is likely to be
372 small.

373 Instead, we suggest that variability in the BIT indices reflects changes in the source of
374 OM. The consistently higher indices in the marls (Fig. 4c) can either be produced by greater
375 terrestrial input of brGDGTs, or by a decrease of marine crenarchaeol production. If the
376 accumulation rate is constant, the concentration of the brGDGTs can be used to distinguish
377 between a terrestrial and marine driver of BIT indices (Smith et al., 2012), i.e. more brGDGTs
378 reflect increased terrestrial input. Here, however, not only is there considerable uncertainty
379 in the accumulation rates through the lithological cycle (Nijenhuis and de Lange, 2000), but
380 also, increased fluvially-derived nutrients could both supply additional terrestrial OM
381 (additional brGDGTs) and also stimulate primary productivity, yielding higher concentrations

382 of crenarchaeol (Zell et al., 2015). GDGT concentrations, therefore, cannot be used to
383 distinguish between these two explanations, because accumulation rates cannot be
384 considered constant (variable brGDGT concentrations before the slump; Fig. 4d). However,
385 increased run-off can explain the increased BIT indices in marls due to increased terrestrial
386 OM input (Fig. 4c), while there is no obvious mechanism for an increase in crenarchaeol
387 production during limestone deposition. Therefore, we argue that, the higher marl BIT indices
388 are indicative of elevated terrigenous OM inputs (e.g. Hopmans et al., 2004).

389 Other OM proxies e.g. $TAR_{n\text{-alkanoic acid}}$ (Fig. 4c and Fig. 5e) and *n*-alkane concentrations
390 have similar but less consistent relationships with lithology (Fig. 5a and Fig. 6). One
391 explanation for these more ambiguous records is that they are more sensitive to changes in
392 relative preservation and within-cycle sedimentation rate changes than BIT indices.
393 Furthermore, these ratios are comprised of end-members (especially the aquatic end-
394 member) with a broad range of terrestrial and marine sources (Meyers and Arnaboldi, 2008).
395 Finally, it appears that *n*-alkyl lipids derive from both fluvial inputs, which would be expected
396 to track other hydrological indicators, and aeolian inputs (see section 4.3) and this mixture of
397 controls further complicates the interpretation of these data. We therefore suggest that BIT
398 indices best record the changes in OM source (i.e. Strong et al., 2012), but that other
399 biomarkers (e.g. $TAR_{n\text{-alkanes}}$; HMW *n*-alkane abundances), also show similar relationships.

400 As a consequence of the insolation control on lithology (Krijgsman et al., 2002), the BIT
401 indices also vary with insolation and are commonly higher during times of high insolation (Fig.
402 4c) when the marls were deposited. Numerical simulations with an ocean-atmosphere-
403 vegetation general circulation model (GCM; Marzocchi et al., 2015 and see supplementary
404 material) show a large increase in run-off from North Africa during the precession minimum
405 (insolation maximum; Fig. 8b), which is consistent with elevated terrigenous OM inputs during

406 marl deposition. A substantial component of this North African fluvial input is delivered to the
407 Eastern Mediterranean via the Nile, which could therefore have exerted a strong control on
408 sedimentary processes at Pissouri (Fig. 1). Given the proximity of Cyprus to the Nile cone, the
409 systematic changes in BIT indices with lithology, record the variability of fluvial input to the
410 Eastern Mediterranean.

411 The relationship between insolation and BIT indices explains only half of its variability
412 (R^2=0.5) and the relationships are weaker within the individual marl and limestone datasets
413 (R^2=0.24, R^2=0.26 respectively). These low regression coefficients suggest that insolation does
414 not generate a systematic gradational change in BIT indices, but instead describes a bi-modal
415 shift in the BIT-insolation relationship between the extremes of the insolation curve. Samples
416 with >0.6 BIT indices derive from parts of the precession cycles associated with insolation
417 >500 W/m^2 (these are all marls) while those with <0.3 BIT indices are associated with
418 insolation of <480 Wm^2 (all but one of these are limestones).

419 ***4.3 Insolation-driven changes in plant inputs inferred from n-alkane isotopes***

420 The correlation between BIT indices and astronomically-controlled lithology suggests
421 that both the quantity and the nature of the terrestrial organic matter being supplied from
422 North Africa could change as the ITCZ shifts position, reflecting changes in the aridity/humidity
423 of the North African catchment. One mechanism for monitoring this is through *n*-alkane $\delta^{13}C$
424 values, which increase in response to the proportion of aridity-adapted C_4 plants in the
425 depositional system (Schwab et al., 2015). There is clear evidence of a global expansion of C_4
426 plants from 8 Ma onwards although this appears to have been delayed by ~2 Myr in the
427 Eastern Mediterranean region (Edwards et al., 2010), post-dating the Pissouri section. These
428 observations dictate caution in the interpretation of even cyclic variations in leaf wax $\delta^{13}C$

values. If the expansion exclusively post-dated the deposition of the study interval, we would expect little leaf wax $\delta^{13}C$ sensitivity. However, this is not the case (Fig. 6). The observed variation in $\delta^{13}C$ could therefore result from two interrelated factors: i) superimposed on this long-term C_3-C_4transition are localised, shorter-term variations, perhaps amplified during the global ecological transition and reflecting regional changes in precipitation and the advantage C_4-plants have over C_3-plants in semi-arid regions (Rommerskirchen et al., 2006); or ii) changes in precipitation driving similar carbon isotopic variation, although of smaller magnitude, in C_3 plants (Diefendorf et al., 2015). Consequently, $\delta^{13}C$ values of *n*-alkanes are expected to be less negative during insolation minima, i.e. limestone deposition, when the ITCZ shifts further south, due either to more enriched C_3 plants and/or a higher proportion of C_4 plants (Fig. 9). However, this is not what we observe in the Pissouri section (Fig. 6), where the $\delta^{13}C$ values for the *n*-alkanes of the limestones are consistently more negative than most (~80%) of the marls (Fig. 6).

It is possible that rather than recording C_3/C_4 vegetation change driven by humidity, the *n*-alkane $\delta^{13}C$ values of the Pissouri samples are responding to other factors, such as temperature (Yamori et al., 2014) or pCO_2 variations (Bolton et al., 2016; Freeman and Colarusso, 2001). However, while we cannot be sure that these low resolution records capture the full range of precessional temperature variation, there is little evidence for pronounced temperature fluctuations with insolation (Fig. 7) that could account for the pattern of *n*-alkane $\delta^{13}C$ observed (Fig. 6). Equally, although there is evidence of pCO_2 decline during the Late Miocene to Early Pliocene (Bolton et al., 2016), the resolution of this record is far too low (4 samples covering 6-8 Myr) to provide any indication that precessional fluctuations in pCO_2 could account for the *n*-alkane $\delta^{13}C$ record at Pissouri.

To explore this further, we have compared our data with inferred insolation assuming

453 little pCO_2 variations, and this reveals $\delta^{13}C$ variations within and between the two lithologies.
454 Within the limestone dataset, there is a clear positive relationship between insolation and the
455 carbon isotopic composition of the long-chain *n*-alkanes, especially *n*-C_{29} and *n*-C_{31} (Fig. 10).
456 It appears that at higher insolation (between 480 and 500 W/m^2), $\delta^{13}C$ values become
457 relatively stable, such that figure 10 shows two possible linear regressions for the relationship
458 between insolation and *n*-alkane $\delta^{13}C$ values based on either all or a subset of the limestone
459 data. The carbon isotopic compositions of the marls do not lie on the same insolation-$\delta^{13}C$
460 regression line as the limestones, but deviate from it towards more negative values (Fig. 10)
461 and show no systematic relationship with insolation.
462 As discussed above, the positive relationship between insolation and *n*-alkane $\delta^{13}C$
463 values in the limestones is unexpected, differing with model simulations of decreased rainfall
464 and expansion of C_4 plants during insolation minima (Fig. 9). By extension, it is apparently
465 inconsistent with our BIT indices which indicated decreased terrestrial OM inputs (i.e.
466 decreased run-off) during insolation minima. Instead, the insolation-$\delta^{13}C$ relationship during
467 the limestone deposition interval of each precessional cycle (e.g. during precession maxima
468 and insolation minima), can be explained by enhanced aeolian transport of *n*-alkanes from
469 the northern margin of the Mediterranean which experienced more arid conditions during
470 insolation maxima (Fig. 9; Marzocchi et al., 2015 and see supplementary material). Such an
471 interpretation is reflected in the vegetation changes seen in the GCM simulations in the
472 Anatolian Plateau (Fig.9); therefore, it appears that the *n*-alkane $\delta^{13}C$ records in the limestones
473 document a persistent source from the north that experienced changing vegetation, where,
474 in contrast with North Africa, there was more precipitation during insolation minima than
475 insolation maxima.
476 This relationship, however, only holds during the extreme part of the precession cycle

that includes the insolation minima. We suggest that during this interval, when run-off from North Africa was presumably lower (Fig. 4), Pissouri was largely unaffected by North African run-off and aeolian input dominated the terrestrially-derived organic matter incorporated into the sediment. During insolation maxima, by contrast, the *n*-alkanes from the tropical rain forests of North Africa (Holtvoeth et al., 2003) supplied the Pissouri depositional system via enhanced Nile River input (Fig.9). This drove the *n*-alkane $\delta^{13}C$ values lower (Fig. 10) overprinting the signal from the Anatolian Plateau.

4.4 Long-term trends

Continuous dry environments have been postulated for the lead up to the MSC (Fauquette et al., 2006), inferred from Eastern Mediterranean pollen records. These show an increase in *Pinus* and *Cthaya* and a decrease in tropical and sub-tropical taxa, which Faquette et al. (2006) attribute to sea-level change and associated coastline variations. The increase of nonacosan-10-ol concentrations which are thought to derive from pine trees (Jetter and Riederer, 1995) at the top of the section could also therefore indicate a sea-level fall (Fig. 5c).

The dry conditions inferred from the pollen data are consistent with the small increase in *n*-alkane $\delta^{13}C$ values above the slump layer (Fig. 6), especially in the longest *n*-alkanes (C_{33}), that may indicate an increase in the proportion of C_4-plants due to increasing aridity or an increase in CO_2; both are favourable for a C_4 plant expansion (Freeman and Colarusso, 2001; Bolton et al., 2016; Huang et al., 2007). It is also consistent with the long-term decrease in limestone BIT indices (Fig. 4c), perhaps suggesting a decrease in run-off during the dry extreme of the precession cycle.

However, the BIT record exhibits additional complexity, with three major trends/shifts in the 600 kyr preceding the MSC: first, the decrease in limestone BIT indices; second, the

500 sharp decrease in marl BIT directly underneath the slump interval; and third, the increase in
501 marl BIT above the slump interval (Fig. 4c). The long-term decrease in BIT indices probably
502 reflects a gradual decrease of terrestrial OM inputs associated with increasing aridity during
503 the 500 kyr before the onset of the MSC, but an increase in crenarchaeol input cannot be
504 excluded (Fig. 4c). The concentrations of *n*-alkanes also exhibit a long-term decline, but reach
505 their lowest values below the slump layer (Fig. 5b) before increasing in the upper part of the
506 section; $TAR_{n\text{-alkanoic-acids}}$ exhibit similar trends. Therefore, in the final ~100 kyr before the MSC,
507 there appears to be divergence in the behaviour of different terrigenous OM inputs.
508 Marine faunal and floral data from Pissouri provides some insights as to the causes of
509 these long-term changes and the environmental conditions that influenced Pissouri.
510 Kouwenhoven et al. (2006) document a collapse in nannoflora at about 20 m (e.g. 6.25 Ma,
511 where the marl BIT indices decline; Fig. 5e) and a recovery just above the slump. Those
512 authors suggest that the abrupt decline in nannoflora may have been caused by a salinity
513 increase. The decline is associated with a sharp increase in the abundance of the calcareous
514 dinocyst: *Thoracosphaera* (Fig. 5e; Kouwenhoven et al., 2006). This dinocyst has been
515 described from the K/T boundary where its abundance immediately after the boundary has
516 suggested that it survived and then exploited a stressful environment as a result of either
517 considerable warming, fluctuation in salinity and pH, or higher CO_2 (Kouwenhoven et al., 2006
518 and references thierein). Of these possible causes, the occurrence of *Thoracosphaera* at
519 Pissouri probably implies higher and more fluctuating salinity conditions from 6.25 Ma
520 onwards, in line with Mediterranean-wide indicators of rising salinity in the lead up to the
521 MSC (e.g. Sierro et al., 2001). An increase in salinity, if driven by decreased freshwater inputs,
522 would be consistent with the decline in BIT indices, $TAR_{n\text{-alkanes}}$ and nonacosan-10-ol
523 abundances from 6.5 Ma to near the top of the slump at ~6.1 Ma (Fig. 4 and Fig. 5).

524 Immediately above the slump, *Thoracosphaera* abundance drops and the nannoflora
525 diversity and abundance recovers, suggesting a less extreme environment (Kouwenhoven et
526 al., 2006). Less saline conditions are consistent with the sharp increase in marl BIT indices, an
527 increase in $TAR_{n\text{-alkanes}}$ indices and the return to pre-6.25 Ma levels of brGDGT abundance
528 above the slump. The high variability in GDGTs and the sharp drop in marl BIT indices at 6.25
529 Ma (Fig. 4c) are also consistent with fluctuating salinity conditions in the Mediterranean
530 before the onset of the MSC at 5.971 Ma. *Thoracosphera* exhibits a similar increase
531 immediately before the MSC, again indicating increasing salinity.

532 Our new data are consistent with a long-term drying in the surrounding catchment, an
533 associated change in vegetation, a decrease in run-off and an associated increase in
534 Mediterranean salinity. However, the expression of these changes varies between proxy
535 records, perhaps suggesting decoupling of simple rainfall, runoff and salinity relationships. Of
536 course, this is to be expected as the MSC is not thought to have been caused solely by climate
537 change but also tectonic changes impacting the Mediterranean Sea's connection to the
538 Atlantic Ocean (Flecker et al., 2015; Achalhi et al., 2016). It appears that a combination of
539 these processes, strongly modulated by orbital forcing, dictated the evolution of
540 Mediterranean climate in the 600 kyr interval leading up to the MSC.

541 **5 Conclusions**

542 The analysis of biomarker distributions and carbon isotopic compositions in the Pissouri
543 section reveals a strong relationship with lithology and, therefore, they are also inferred to
544 respond to precession-driven insolation variation during the 600 kyr preceding the MSC. The
545 sediments deposited during inferred insolation maxima (marls) contain a greater proportion
546 of terrestrially-derived organic matter than those deposited during insolation minima

(limestones). BIT indices support the hypothesis that the Eastern Mediterranean experienced large changes in run-off from Northern African catchments during each precessional cycle. Leaf wax $\delta^{13}C$ values indicate that North Africa is not the only source of terrestrially-derived organic matter and that Pissouri also received material from the northern margin of the Mediterranean, probably the Anatolian Plateau in Turkey via aeolian inputs. The $\delta^{13}C$ data suggest that this area was characterised by more arid vegetation, which also varied with precession such that more arid conditions prevailed during periods of higher insolation, in line with climate models. This arid material was supplied to Pissouri throughout the succession, but it only dominates the carbon isotope signature of leaf waxes during low insolation when the influence of the Nile was reduced as a result of lower discharge. The long-term trends in the data indicate that the increasing salinity of the looming Messinian Salinity Crisis was already apparent in the Pissouri section in the biomarker data more than 600 kyr before the first gypsum precipitated and was especially clear and influential during the last 100 kyr.

6 Acknowledgments

Data can be accessed via the online supporting information or from author: jp.mayser@bristol.ac.uk. We thank the NERC Life Sciences Mass Spectrometry Facility (Bristol) for analytical support. JPM thanks David Naafs, Gordon Inglis, Sabine Lengger, Megan Rohrssen and the whole MEDGATE team for useful discussions. This work was funded by the People Programme of the European Union's 7th Framework Programme FP7/2007–2013/ under REA grant agreement no. 290201 MEDGATE. RDP also acknowledges the Royal Society Wolfson Research Merit Award and the EU Advanced ERC Grant TGRES. Finally, we thank the two anonymous reviewers for their comments and thoughtful suggestions which improved this manuscript.

7 References

1. Achalhi, M., Münch, P., Cornée, J.-J., Azdimousa, A., Melinte-Dobrinescu, M., Quillévéré, F., Drinia, H., Fauquette, S., Jiménez-Moreno, G., Merzeraud, G., Moussa, A.B., El Kharim, Y., Feddi, N., 2016. The Late Miocene Mediterranean-Atlantic connections through the North Rifian Corridor: New insights from the Boudinar and Arbaa Taourirt basins (northeastern Rif, Morocco). Palaeogeography, Palaeoclimatology, Palaeoecology 459, 131-152. doi: http://dx.doi.org/10.1016/j.palaeo.2016.06.040
2. Bolton, C.T., Hernandez-Sanchez, M.T., Fuertes, M.A., Gonzalez-Lemos, S., Abrevaya, L., Mendez-Vicente, A., Flores, J.A., Probert, I., Giosan, L., Johnson, J., Stoll, H.M., 2016. Decrease in coccolithophore calcification and CO_2 since the middle Miocene. Nature Communications 7, 10284. doi: 10.1038/ncomms10284
3. Bourbonniere, R.A., Meyers, P.A., 1996. Sedimentary geolipid records of historical changes in the watersheds and productivities of Lakes Ontario and Erie. Limnol Oceanogr 41, 352-359.
4. Bray, E.E., Evans, E.D., 1961. Distribution of Normal-Paraffins as a Clue to Recognition of Source Beds. Geochim Cosmochim Ac 22, 2-15. doi: 10.1016/0016-7037(61)90069-2
5. De Jonge, C., Hopmans, E.C., Zell, C.I., Kim, J.-H., Schouten, S., Sinninghe Damsté, J.S., 2014. Occurrence and abundance of 6-methyl branched glycerol dialkyl glycerol tetraethers in soils: Implications for palaeoclimate reconstruction. Geochim Cosmochim Ac 141, 97-112. doi: 10.1016/j.gca.2014.06.013
6. Diefendorf, A.F., Leslie, A.B., Wing, S.L., 2015. Leaf wax composition and carbon isotopes vary among major conifer groups. Geochim Cosmochim Ac 170, 145-156. doi: 10.1016/j.gca.2015.08.018
7. Edwards, E.J., Osborne, C.P., Stromberg, C.A., Smith, S.A., Consortium, C.G., 2010. The origins of C_4 grasslands: integrating evolutionary and ecosystem science. Science 328, 587-591. doi: 10.1126/science.1177216
8. Eglinton, G., Hamilton, R.J., 1967. Leaf epicuticular waxes. Science 156, 1322-1335.
9. Fauquette, S., Suc, J., Bertini, A., Popescu, S., Warny, S., Taoufiq, N., Villa, M., Chikhi, H., Feddi, N., Subally, D., Clauzon, G., Ferrier, J., 2006. How much did climate force the Messinian salinity crisis? Quantified climatic conditions from pollen records in the Mediterranean region. Palaeogeogr Palaeocl 238, 281-301. doi: 10.1016/j.palaeo.2006.03.029
10. Flecker, R., Krijgsman, W., Capella, W., de Castro Martíns, C., Dmitrieva, E., Mayser, J.P., Marzocchi, A., Modestou, S., Lozano, D.O., Simon, D., Tulbure, M., van den Berg, B., van der Schee, M., de Lange, G., Ellam, R., Govers, R., Gutjahr, M., Hilgen, F., Kouwenhoven, T., Lofi, J., Meijer, P., Sierro, F.J., Bachiri, N., Barhoun, N., Alami, A.C., Chacon, B., Flores, J.A., Gregory, J., Howard, J., Lunt, D., Ochoa, M., Pancost, R., Vincent, S., Yousfi, M.Z., 2015. Evolution of the Late Miocene Mediterranean-Atlantic gateways and their impact on regional and global environmental change. Earth-Sci Rev. doi: 10.1016/j.earscirev.2015.08.007
11. Freeman, K.H., Colarusso, L.A., 2001. Molecular and isotopic records of C_4 grassland expansion in the Late Miocene. Geochim Cosmochim Ac 65, 1439-1454. doi: 10.1016/s0016-7037(00)00573-1
12. Hilgen, F.J., Krijgsman, W., Langereis, C.G., Lourens, L.J., 1997. Breakthrough made in dating of the geological record. Eos, Transactions American Geophysical Union 78, 285. doi: 10.1029/97eo00186
13. Holtvoeth, J., Wagner, T., Schubert, C.J., 2003. Organic matter in river-influenced continental margin sediments: The land-ocean and climate linkage at the Late Quaternary Congo fan (ODP Site 1075). Geochemistry, Geophysics, Geosystems 4. doi: 10.1029/2003gc000590
14. Hopmans, E.C., Schouten, S., Pancost, R.D., van der Meer, M.T., Sinninghe Damste, J.S., 2000. Analysis of intact tetraether lipids in archaeal cell material and sediments by high performance liquid chromatography/atmospheric pressure chemical ionization mass spectrometry. Rapid Commun Mass Spectrom 14, 585-589. doi: 10.1002/(SICI)1097-0231(20000415)14:7<585::AID-RCM913>3.0.CO;2-N
15. Hopmans, E.C., Weijers, J.W.H., Schefuss, E., Herfort, L., Damste, J.S.S., Schouten, S., 2004. A novel proxy for terrestrial organic matter in sediments based on branched and isoprenoid tetraether lipids. Earth Planet Sc Lett 224, 107-116. doi: 10.1016/j.epsl.2004.05.012
16. Huang, Y., Clemens, S.C., Liu, W., Wang, Y., Prell, W.L., 2007. Large-scale hydrological change drove the late Miocene C_4 plant expansion in the Himalayan foreland and Arabian Peninsula. Geology 35, 531. doi: 10.1130/G23666A.1
17. Huguet, C., Kim, J.-H., de Lange, G.J., Sinninghe Damsté, J.S., Schouten, S., 2009. Effects of long term oxic degradation on the, TEX_{86} and BIT organic proxies. Organic Geochemistry 40, 1188-1194. doi: 10.1016/j.orggeochem.2009.09.003

18. Huguet, C., Hopmans, E.C., Febo-Ayala, W., Thompson, D.H., Sinninghe Damsté, J.S., Schouten, S., 2006. An improved method to determine the absolute abundance of glycerol dibiphytanyl glycerol tetraether lipids. Org Geochem 37, 1036-1041. doi: 10.1016/j.orggeochem.2006.05.008
19. Jetter, R., Riederer, M., 1995. In vitro Reconstitution of Epicuticular Wax Crystals: Formation of Tubular Aggregates by Long-Chain Secondary Alkanediols. Botanica Acta 108, 111-120. doi: 10.1111/j.1438-8677.1995.tb00840.x
20. Kidd, R.B., Cita, M.B., Ryan, W.B.F., 1978. Stratigraphy of Eastern Mediterranean sapropel sequences recovered during DSDP 42A and their palaeoenvioromental significance.
21. Kim, J.H., van der Meer, J., Schouten, S., Helmke, P., Willmott, V., Sangiorgi, F., Koc, N., Hopmans, E.C., Damste, J.S.S., 2010. New indices and calibrations derived from the distribution of crenarchaeal isoprenoid tetraether lipids: Implications for past sea surface temperature reconstructions. Geochimica Et Cosmochimica Acta 74, 4639-4654. doi: 10.1016/j.gca.2010.05.027
22. Kouwenhoven, T.J., Morigi, C., Negri, A., Giunta, S., Krijgsman, W., Rouchy, J.M., 2006. Paleoenvironmental evolution of the eastern Mediterranean during the Messinian: Constraints from integrated microfossil data of the Pissouri Basin (Cyprus). Mar Micropaleontol 60, 17–44. doi: 10.1016/j.marmicro.2006.02.005
23. Kouwenhoven, T.J, Hilgen, F. J., van der Zwaan, G. J.,2003. Late Tortonian-early Messinian stepwise disruption of the Mediterranean-Atlantic connections: constraints from benthic foraminiferal and geochemical data. Palaeogeography Palaeoclimatology Palaeoecology 198, 303-319. doi: 10.1016/S0031-0182(03)00482-3
24. Krijgsman, W., Blanc-Valleron, M.M., Flecker, R., Hilgen, F.J., Kouwenhoven, T.J., Merle, D., Orszag-Sperber, F., Rouchy, J.M., 2002. The onset of the Messinian salinity crisis in the Eastern Mediterranean (Pissouri Basin, Cyprus). Earth Planet Sc Lett 194, 299-310. doi: 10.1016/S0012-821x(01)00574-X
25. Kutzbach, J.E., Chen, G., Cheng, H., Edwards, R.L., Liu, Z., 2014. Potential role of winter rainfall in explaining increased moisture in the Mediterranean and Middle East during periods of maximum orbitally-forced insolation seasonality. Climate Dynamics 42, 1079-1095. doi: 10.1007/s00382-013-1692-1
26. Larrasoaña J.C., Roberts, A. P., Rohling, E. J., 2013. Dynamics of Green Sahara Periods and Their Role in Hominin Evolution. PLoSONE 8, doi: 10.1371/journal.pone.0076514
27. Laskar, J., Robutel, P., Joutel, F., Gastineau, M., Correia, A.C.M., Levrard, B., 2004. A long-term numerical solution for the insolation quantities of the Earth. Astronomy and Astrophysics 428, 261-285. doi: 10.1051/0004-6361:20041335
28. Manzi, V., Gennari, R., Hilgen, F., Krijgsman, W., Lugli, S., Roveri, M., Sierro, F.J., 2013. Age refinement of the Messinian salinity crisis onset in the Mediterranean. Terra Nova 25, 315-322. doi: 10.1111/Ter.12038
29. Marzocchi, A., Lunt, D.J., Flecker, R., Bradshaw, C.D., Farnsworth, A., Hilgen, F.J., 2015. Orbital control on Late Miocene climate and the North African monsoon: insight from an ensemble of sub-precessional simulations. Climate of the Past Discussions 11, 2181-2237. doi: 10.5194/cpd-11-2181-2015
30. Meyers, P.A., Arnaboldi, M., 2008. Paleoceanographic implications of nitrogen and organic carbon isotopic excursions in mid-Pleistocene sapropels from the Tyrrhenian and Levantine Basins, Mediterranean Sea. Palaeogeogr Palaeocl 266, 112-118. doi: 10.1016/j.palaeo.2008.03.018
31. Nijenhuis, I.A., de Lange, G.J., 2000. Geochemical constraints on Pliocene sapropel formation in the eastern Mediterranean. Mar Geol 163, 41-63. doi: 10.1016/s0025-3227(99)00093-6
32. O'Leary, M.H., 1981. Carbon isotope fractionation in plants. Phytochemistry 20, 553-567. doi: 10.1016/0031-9422(81)85134-5
33. Peterse, F., van der Meer, J., Schouten, S., Weijers, J.W.H., Fierer, N., Jackson, R.B., Kim, J.-H., Sinninghe Damsté, J.S., 2012. Revised calibration of the MBT–CBT paleotemperature proxy based on branched tetraether membrane lipids in surface soils. Geochim Cosmochim Ac 96, 215-229. doi: 10.1016/j.gca.2012.08.011
34. Rohling, E.J., Marino, G., Grant, K.M., 2015. Mediterranean climate and oceanography, and the periodic development of anoxic events (sapropels). Earth-Sci Rev 143, 62-97. doi: 10.1016/j.earscirev.2015.01.008
35. Rommerskirchen, F., Eglinton, G., Dupont, L., Rullkotter, J., 2006. Glacial/interglacial changes in southern Africa: Compound-specific $\delta^{13}C$ land plant biomarker and pollen records from southeast Atlantic continental margin sediments. Geochemistry Geophysics Geosystems 7. doi: Artn Q0801010.1029/2005gc001223

36. Rossignol-Strick, M., 1985. Mediterranean Quaternary Sapropels, an Immediate Response of the African Monsoon to Variation of Insolation. Palaeogeogr Palaeocl 49, 237-263. doi: 10.1016/0031-0182(85)90056-2
37. Schouten, S., Hopmans, E.C., Sinninghe Damsté, J.S., 2013. The organic geochemistry of glycerol dialkyl glycerol tetraether lipids: A review. Org Geochem 54, 19-61. doi: 10.1016/j.orggeochem.2012.09.006
38. Schwab, V.F., Garcin, Y., Sachse, D., Todou, G., Séné, O., Onana, J.-M., Achoundong, G., Gleixner, G., 2015. Effect of aridity on $\delta^{13}C$ and δD values of C_3 plant- and C_4 graminoid-derived leaf wax lipids from soils along an environmental gradient in Cameroon (Western Central Africa). Org Geochem 78, 99-109. doi: 10.1016/j.orggeochem.2014.09.007
39. Sierro, F.J., Hilgen, F.J., Krijgsman, W., Flores, J.A., 2001. The Abad composite (SE Spain): a Messinian reference section for the Mediterranean and the APTS. Palaeogeogr Palaeocl 168, 141-169. doi: 10.1016/S0031-0182(00)00253-4
40. Sinninghe Damsté, J.S., Schouten, S., Hopmans, E.C., van Duin, A.C., Geenevasen, J.A., 2002. Crenarchaeol: the characteristic core glycerol dibiphytanyl glycerol tetraether membrane lipid of cosmopolitan pelagic crenarchaeota. J Lipid Res 43, 1641-1651. doi: 10.1194/jlr.M200148-JLR200
41. Smith, R.W., Bianchi, T.S., Li, X., 2012. A re-evaluation of the use of branched GDGTs as terrestrial biomarkers: Implications for the BIT Index. Geochim Cosmochim Ac 80, 14-29. doi 10.1016/j.gca.2011.11.025
42. Strong, D.J., Flecker, R., Valdes, P.J., Wilkinson, I.P., Rees, J.G., Zong, Y.Q., Lloyd, J.M., Garrett, E., Pancost, R.D., 2012. Organic matter distribution in the modern sediments of the Pearl River Estuary. Org Geochem 49, 68-82. doi: 10.1016/j.orggeochem.2012.04.011
43. Sugden, W., McKerrow, W.S., 1962. The Composition of Marls and Limestones in the Great Oolite Series of Oxfordshire. Geological Magazine 99, 363. doi: 10.1017/s0016756800058477
44. Tierney, J.E., Tingley, M.P., 2015. A TEX_{86} surface sediment database and extended Bayesian calibration. Scientific data 2, 150029. doi: 10.1038/sdata.2015.29
45. Toucanne, S., Angue Minto'o, C.M., Fontanier, C., Bassetti, M.-A., Jorry, S.J., Jouet, G., 2015. Tracking rainfall in the northern Mediterranean borderlands during sapropel deposition. Quaternary Sci Rev 129, 178-195. doi: 10.1016/j.quascirev.2015.10.016
46. Tzanova, A., Herbert, T.D., Peterson, L., 2015. Cooling Mediterranean sea surface temperatures during the Late Miocene provide a climate context for evolutionary transitions in Africa and Eurasia. Earth Planet Sc Lett 419, 71-80. doi: 10.1016/j.epsl.2015.03.016
47. Weijers, J.W.H., Schouten, S., van den Donker, J.C., Hopmans, E.C., Damste, J.S.S., 2007. Environmental controls on bacterial tetraether membrane lipid distribution in soils. Geochim Cosmochim Ac 71, 703-713. doi: 10.1016/j.gca.2006.10.003
48. Yamori, W., Hikosaka, K., Way, D.A., 2014. Temperature response of photosynthesis in C_3, C_4, and CAM plants: temperature acclimation and temperature adaptation. Photosynth Res 119, 101-117. doi: 10.1007/s11120-013-9874-6
49. Yang, H., Pancost, R.D., Dang, X.Y., Zhou, X.Y., Evershed, R.P., Xiao, G.Q., Tang, C.Y., Gao, L., Guo, Z.T., Xie, S.C., 2014. Correlations between microbial tetraether lipids and environmental variables in Chinese soils: Optimizing the paleo-reconstructions in semi-arid and arid regions. Geochim Cosmochim Ac 126, 49-69. doi: 10.1016/j.gca.2013.10.041
50. Zell, C., Kim, J.-H., Dorhout, D., Baas, M., Sinninghe Damsté, J.S., 2015. Sources and distributions of branched tetraether lipids and crenarchaeol along the Portuguese continental margin: Implications for the BIT index. Continental Shelf Research. doi: 10.1016/j.csr.2015.01.006

8 Figures

Figure 1: Map showing the inflow of the Nile into the Mediterranean and the location of the Pissouri Section on Cyprus (34°40'01.9"N; 32°38'48.8"E). A photograph of the section before it was sprayed with concrete is given on the right.

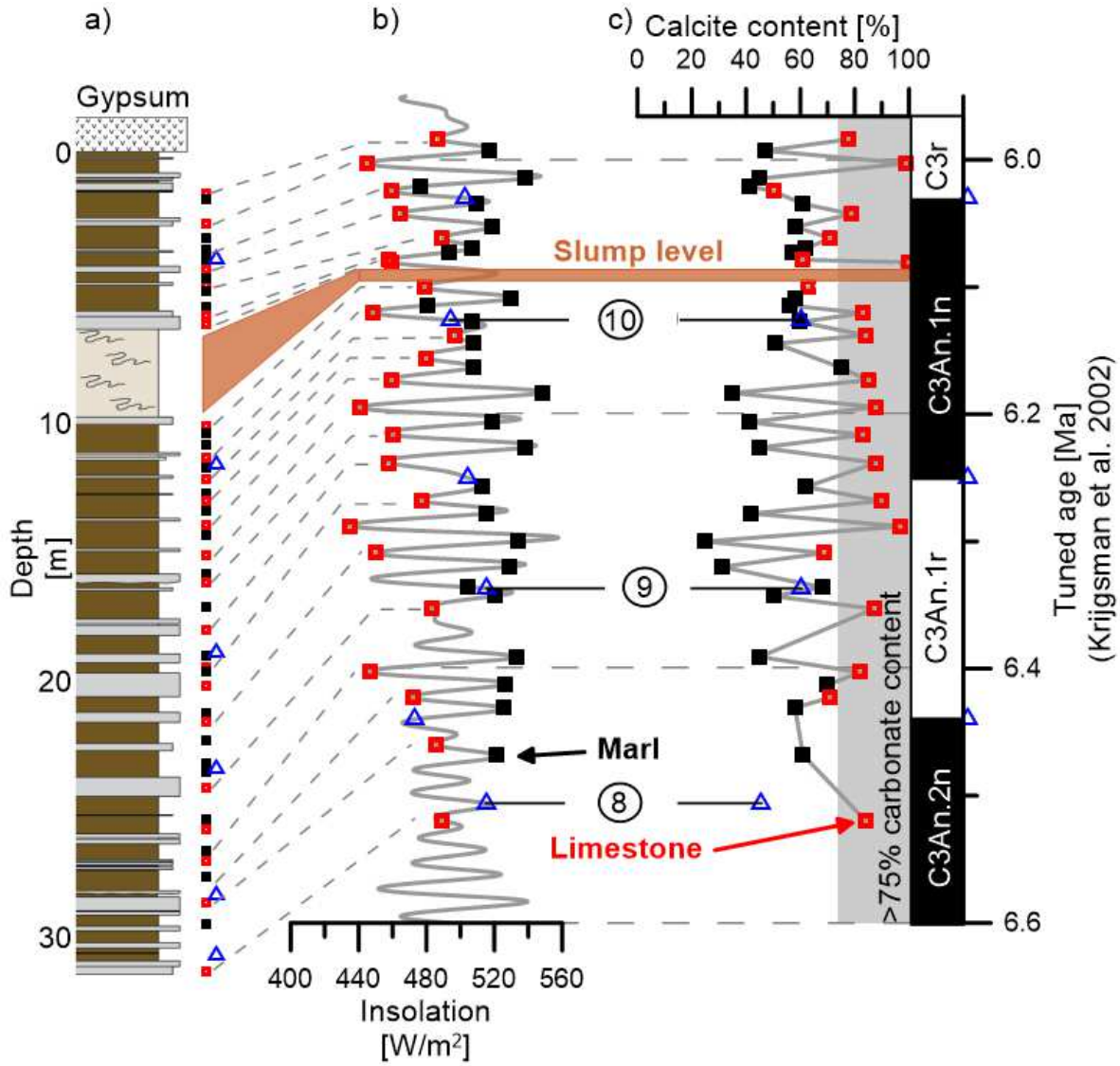

733

734 Figure 2: Schematic log of the Pissouri section (a) with alternating harder (grey and
735 softer (brown)layers alongside (b) the insolation curve (Laskar et al., 2004) and (c) the calcium
736 carbonate content of the sediment which was used for astronomical tuning of the section
737 (Krijgsman et al., 2002). The biostratigraphic tie points (blue triangles) shown from Krijgsman
738 et al. (2002) are: (8) the LO of the *G. miotumida* group (6.506 Ma); (9) the sinistral/dextral
739 coiling change of *Neogloboquadrina acostaensis* (6.337 Ma); and (10) the first infux (>80%) of
740 sinistral neogloboquadrinids (6.126 Ma). The palaeomagnetic tie points (blue triangles) are
741 C3r-C3An.1n (6.03 Ma) C3An.1n-C3An.1r (6.25 Ma) C3An.1r-C3An.2n (6.44 Ma; Krijgsman et
742 al., 2002). The vertical grey bar reflects >75% carbonate content, the formal definition of a

743 limestone (Sugden and McKerrow, 1962). A slump layer (brown bar) interrupts the cyclic
744 limestone-marl alternations between 7 and 10 m depth (Krijgsman et al., 2002).
745

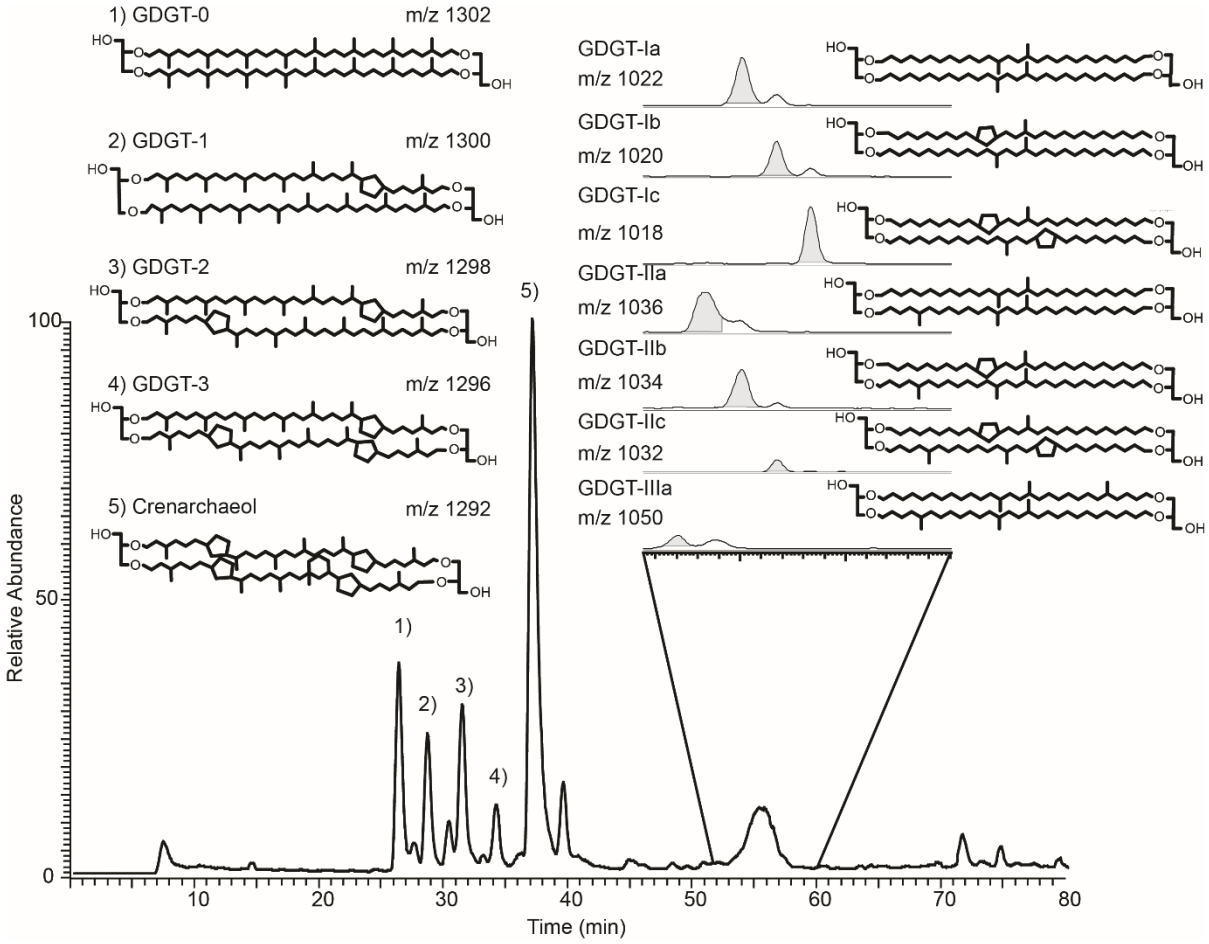

746

747 Figure 3: Representative HPLC-APCI-MS chromatogram of a Pissouri limestone (RF-7018;

748 data table) showing both br- and iGDGTs with their respective *m/z*. Note that the brGDGT

749 peak in this particular total ion content trace is dominated by GDGT-Ia

750

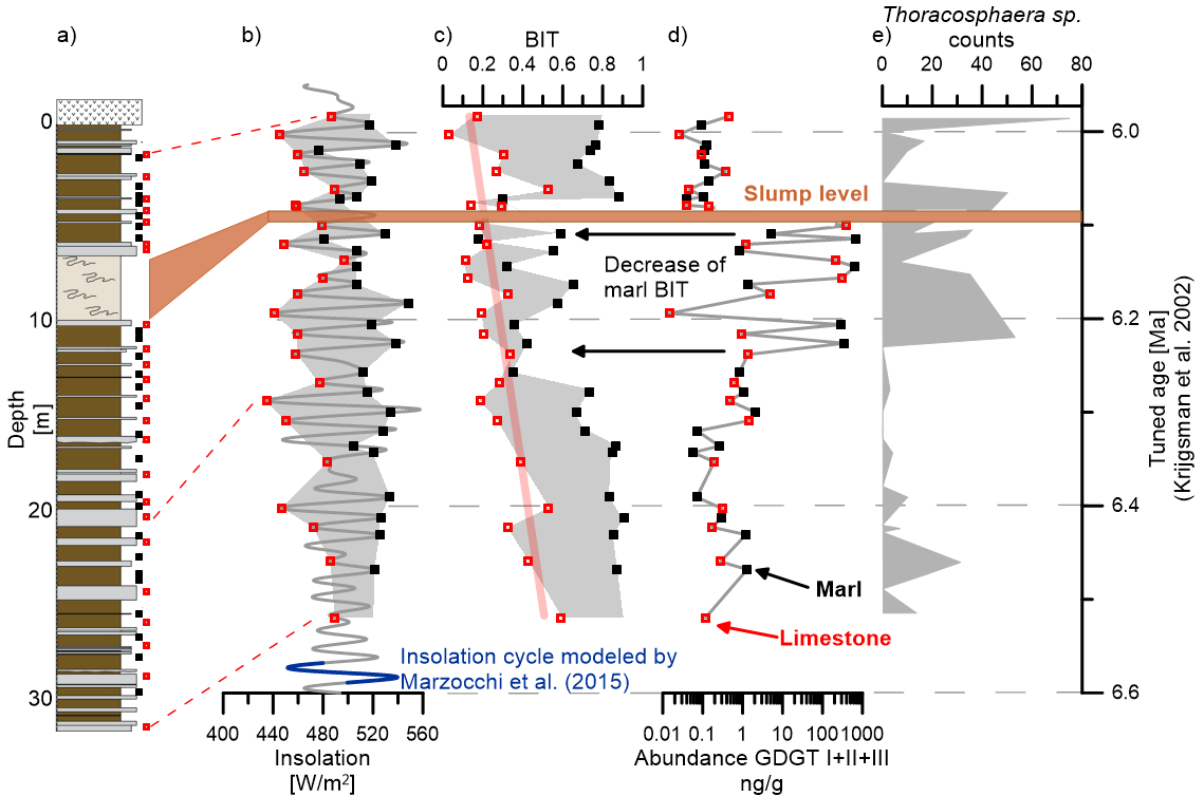

Figure 4: A schematic log (a) of the Pissouri section (Krijgsman et al., 2002) showing sampled levels: limestones (red squares) and marls (black squares). Aligned with the log are (b) the 65N insolation curve (Laskar et al., 2004) with the specific cycle used for the General Circulation Model simulations indicated in blue (Marzocchi et al., 2015), (c) BIT indices, including the long-term trend through the limestone data, (d) brGDGT abundances and (e) counts for the calcareous dinocyst *Thoracosphaera sp.* (Kouwenhoven et al., 2006).

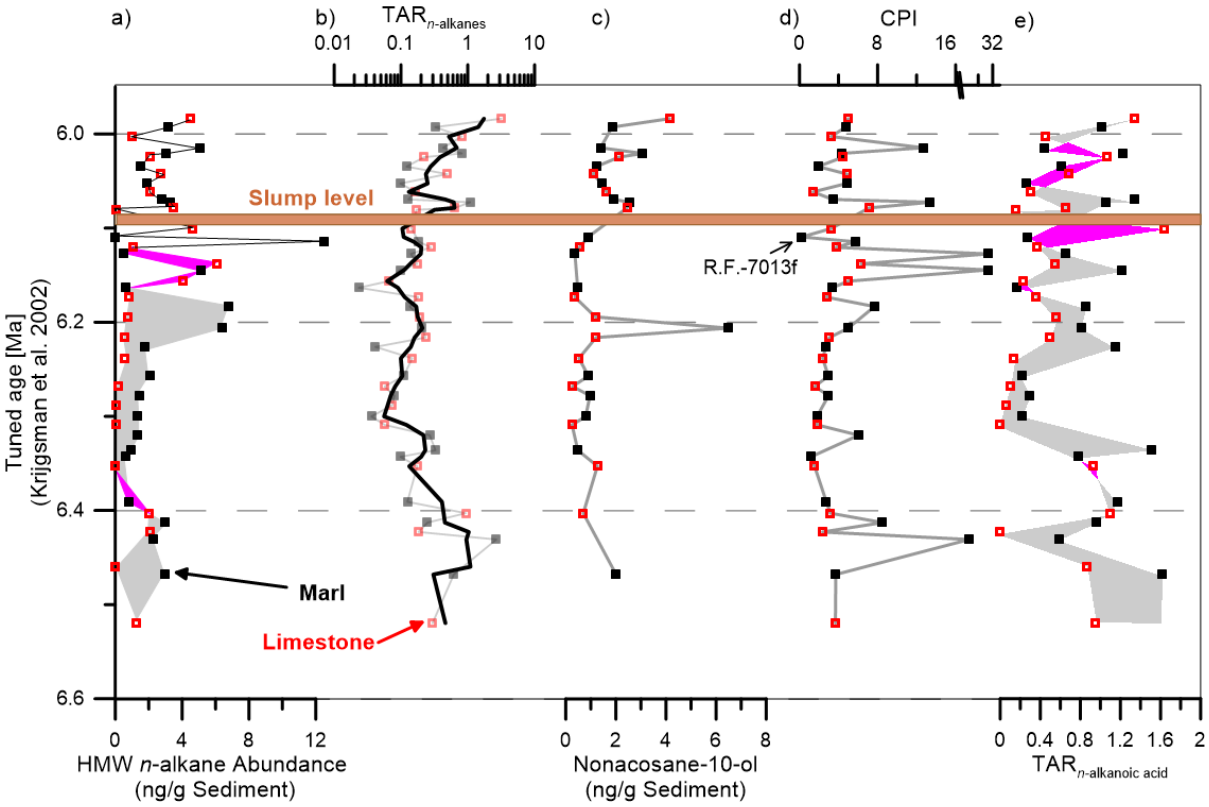

759

760 Figure 5: Alkyl biomarker records through the Pissouri section including (a) HMW *n*-

761 alkane (C_{29}+C_{31}+C_{33}) concentrations; (b) the $TAR_{n\text{-alkanes}}$ with a three point running average; the

762 (c) nonacosan-10-ol concentrations; (d) the CPI of the *n*-alkanes with the excluded sample

763 R.F.713f highlighted; and (e) the $TAR_{n\text{-alkanoic acid}}$. Grey shading indicates higher marl values

764 relative to limestones, whereas magenta indicates higher values for limestones than adjacent

765 marls.

766

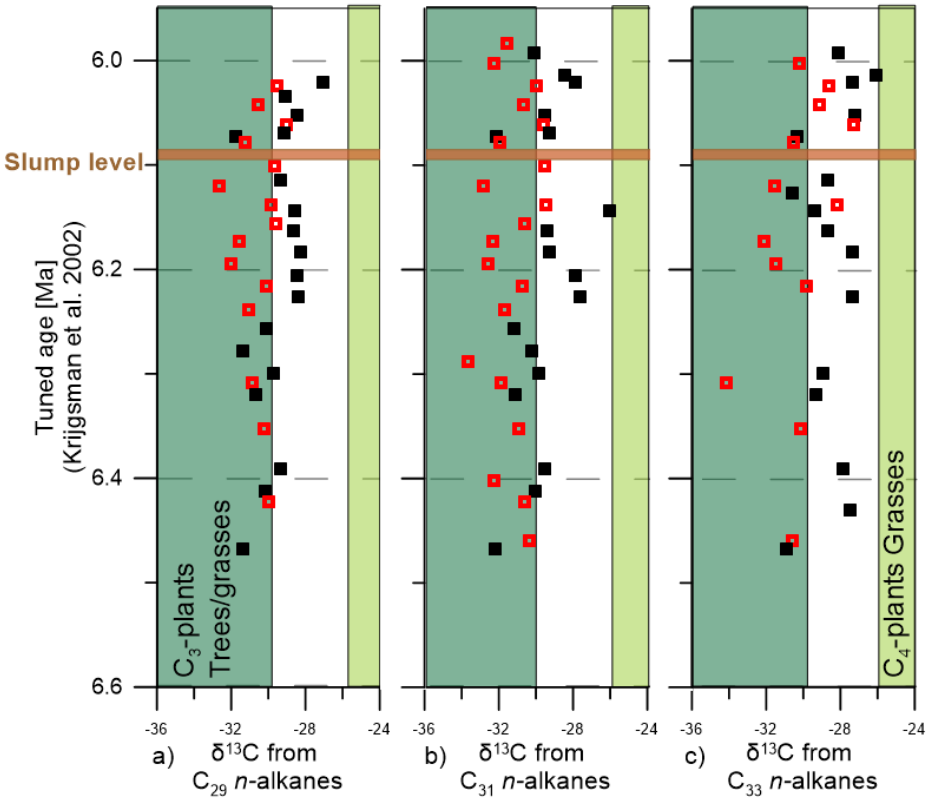

767

768 Figure 6: Age profiles of the (a) C_{29}, (b) C_{31}, and (c) C_{33} *n*-alkane $\delta^{13}C$ values as well as
769 that of (d) the combined abundances of those three *n*-alkanes. The stable carbon isotopic
770 composition of leaf waxes are dependent on the biosynthetic pathway of the source plant
771 (O'Leary, 1981). A typical distribution for $\delta^{13}C$ values of C_{29}-C_{31} *n*-alkanes from leaf waxes of
772 C_3 and C_4 plants is given as green shading (modified after Rommerskirchen et al., 2006).

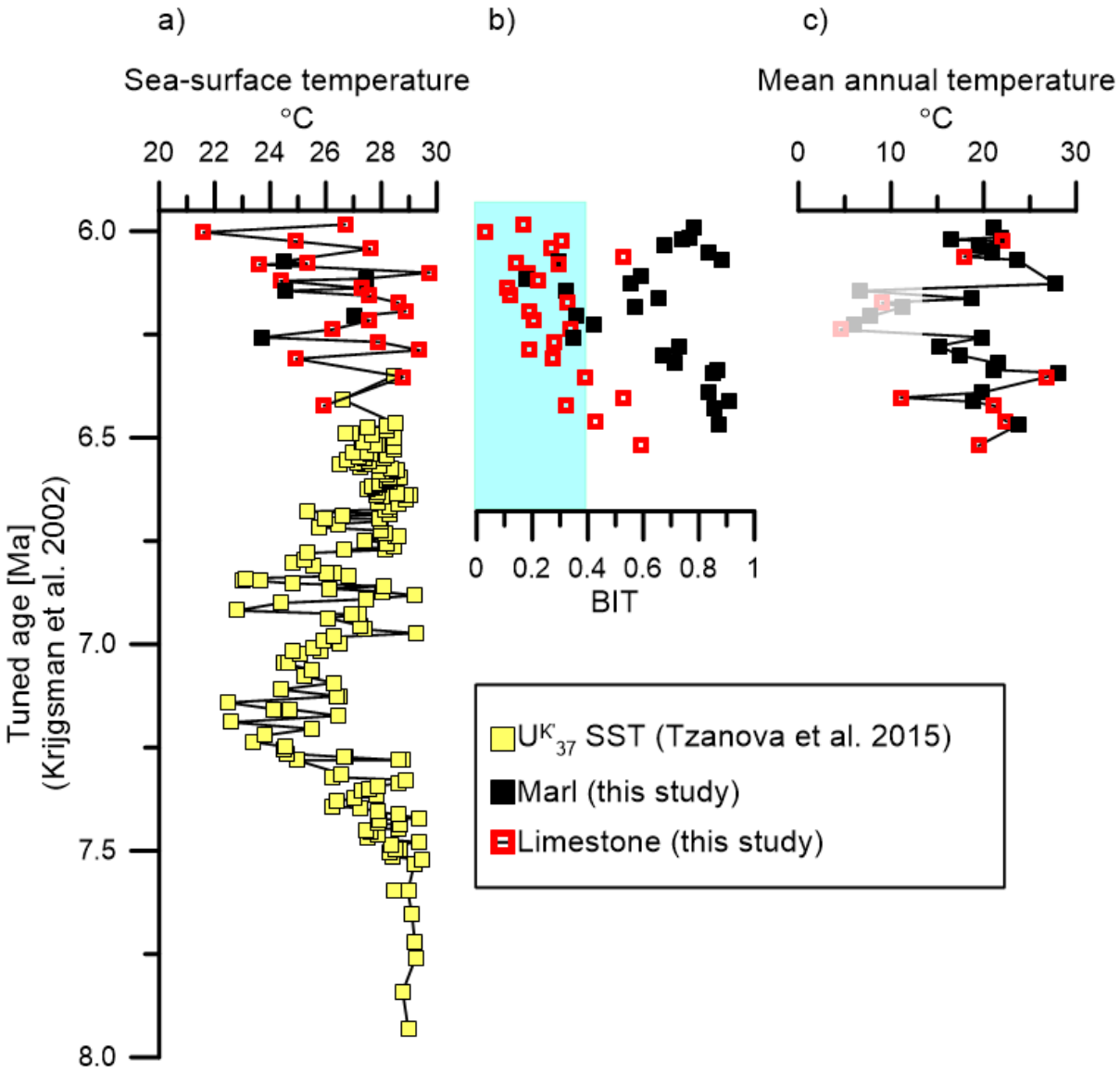

773

774 Figure 7: The SST profile (a) derived from GDGTs (TEX_{86}, this study) at Pissouri and

775 alkenones ($U^{K'}37$, Tzanova et al., 2015) from Monte dei Corvi, Italy. TEX_{86} data are limited to

776 those samples with BIT < 0.4 from Pissouri. Also shown are limestone and marl BIT indices (b;

777 with BIT <0.4 shaded in turquoise) and (c) limestone and marl MBT'/CBT-derived MAT (Peterse

778 et al., 2012) for samples with BIT>0.3. The shaded area in grey marks the decrease in marl BIT

779 area.

780

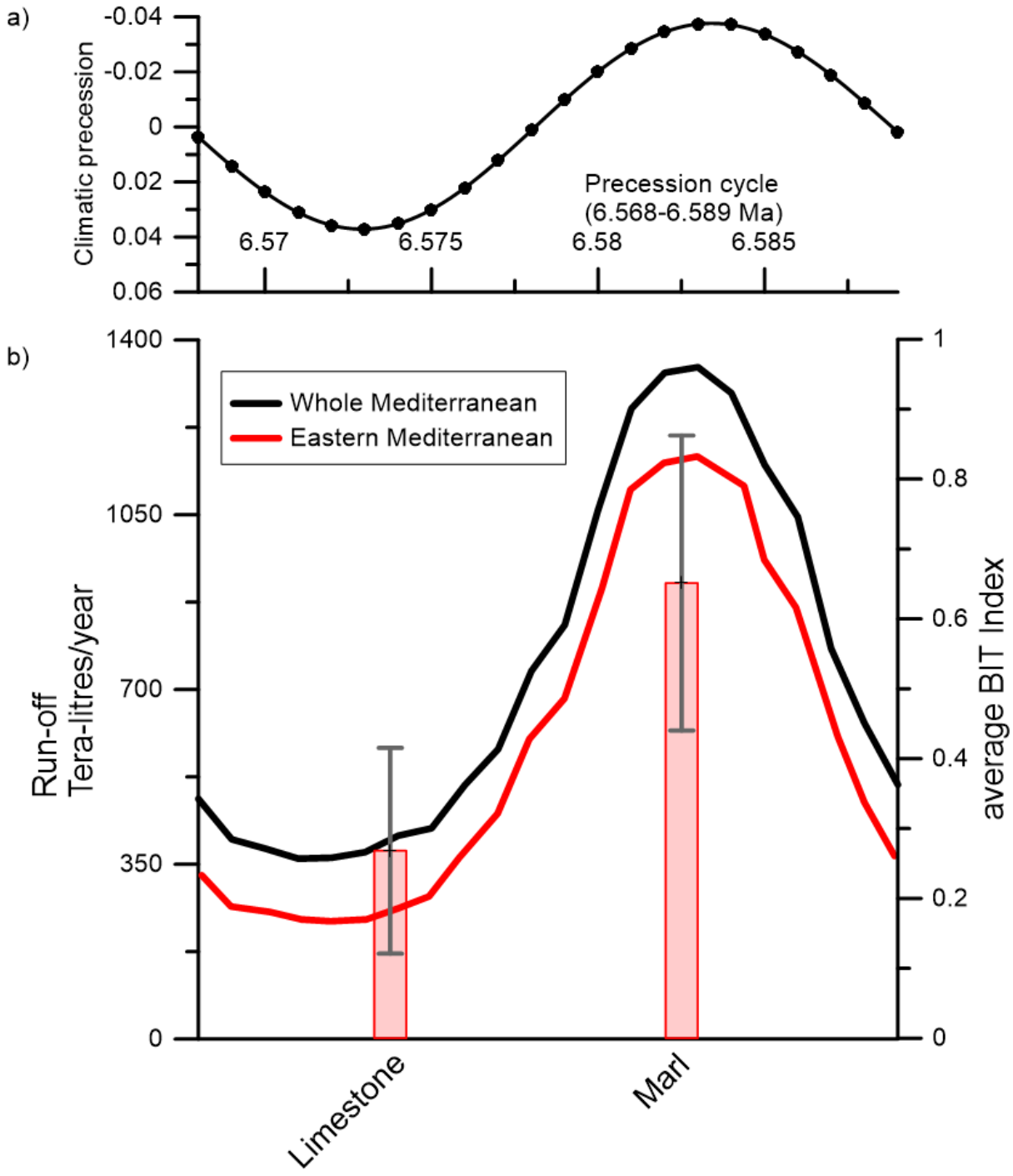

781

782 Figure 8: Climate Model-derived run-off into the Mediterranean as a whole (black line)
783 and Eastern Mediterranean (red line) and its relationship with precession-forced insolation
784 over one precession cycle (Marzocchi et al., 2015 and see supplementary material). The bar
785 chart shows the average and standard deviation of the BIT indices in the limestones and the
786 marls throughout the entire section.

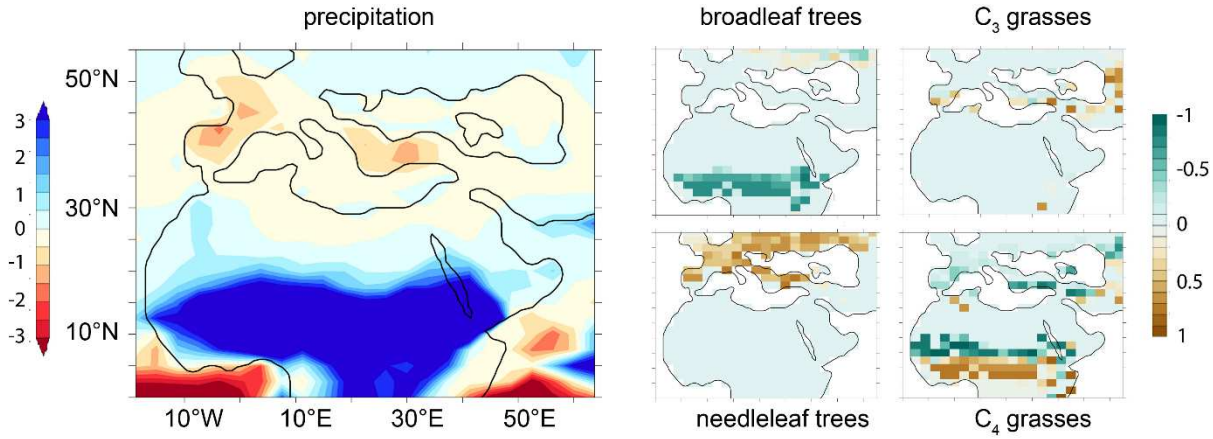

787

788 Figure 9: Precipitation differences between precession minima (insolation maxima) and
789 precession maxima (insolation minima) across N. Africa and the Mediterranean, simulated
790 using HadCM3L with coupled ocean, atmosphere and vegetation (Marzocchi et al., 2015). The
791 four smaller panels show vegetation changes between precession minima and precession
792 maxima for broadleaf trees, needle leaf trees, C3-plants and C4-plants (Marzocchi et al., 2015
793 and see supplementary material).

794

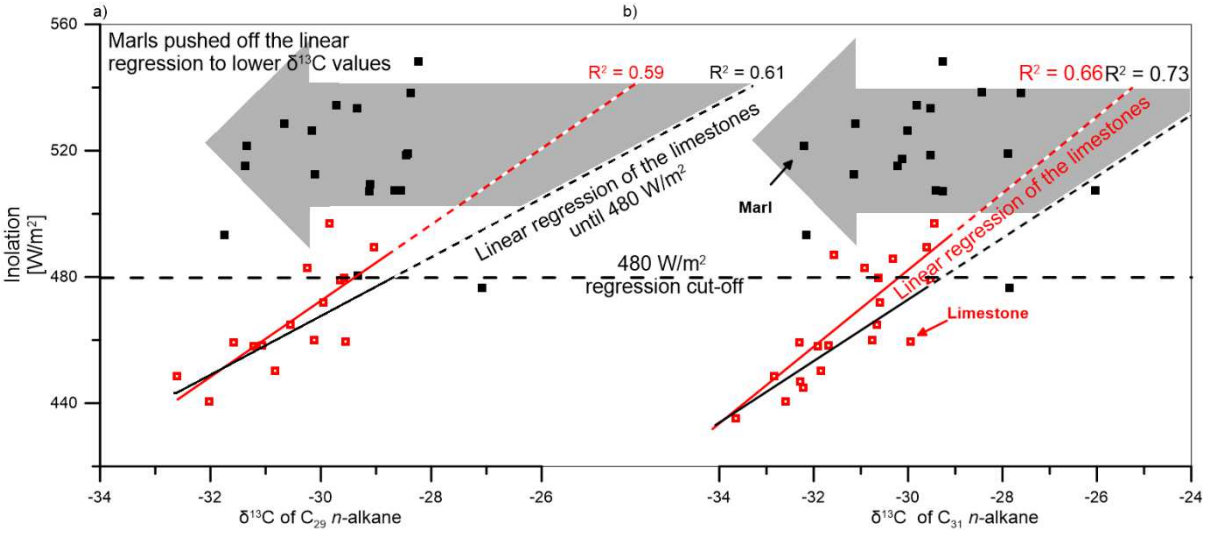

795

796 Figure 10: Cross-plot of insolation versus leaf wax $\delta^{13}C$ values, showing the different
797 relationships for the marls (black) and the limestones (red) for a) C_{29} and b) C_{31} *n*-alkanes. The
798 linear regressions of the limestones are indicated (red for all limestones and black for
799 limestones beneath 480 W/m^2, above which the relationship appears to break down). Both
800 regressions are extrapolated to higher insolation by dashed lines. The offset of the leaf wax
801 $\delta^{13}C$ values to lower values in the marls is indicated with the grey arrow. The absolute
802 insolation is derived from astronomical tuning of the Pissouri Section (Krijgsman et al., 2002).